AGU PUBLICATIONS

JGR

Journal of Geophysical Research: Earth Surface

RESEARCH ARTICLE

10.1002/2013JF002999

Key Points:
- Intermediate scales are crucial for the asymmetry of spatial bed elevation data
- Asymmetry in spatial data is different in nature to bed elevation time series
- Both spatial and temporal data become more complex as discharge increases

Correspondence to:
C. J. Keylock,
c.keylock@sheffield.ac.uk

Citation:
Keylock, C. J., A. Singh, and E. Foufoula-Georgiou (2014), The complexity of gravel bed river topography examined with gradual wavelet reconstruction, *J. Geophys. Res. Earth Surf.*, *119*, 682–700, doi:10.1002/2013JF002999.

Received 1 OCT 2013
Accepted 24 FEB 2014
Accepted article online 26 FEB 2014
Published online 28 MAR 2014

The complexity of gravel bed river topography examined with gradual wavelet reconstruction

C. J. Keylock[1], Arvind Singh[2], and E. Foufoula-Georgiou[2]

[1]Sheffield Fluid Mechanics Group and Department of Civil and Structural Engineering, University of Sheffield, Sheffield, UK, [2]Department of Civil Engineering, St. Anthony Falls Laboratory, and National Center for Earth-Surface Dynamics, University of Minnesota, Minneapolis, Minnesota, USA

Abstract This study analyzes the nonlinear nature of gravel bed elevation data series obtained in a large scale flume facility for four different discharges, including spatial transect series and temporal series at a fixed location. The goals are to infer the degree of complexity, to assess the scales and features in the signals that mostly contribute to this complexity, and to discern the difference in the manner in which this complexity is expressed in time and space. The asymmetry series (magnitude of the first-order derivative of the signal over a separation distance, Δ, raised to the third power) of the bed elevation data forms the basis of our nonlinearity analysis. An important and novel dimension is the adoption of a recently introduced approach to surrogate data generation, gradual wavelet reconstruction. This produces partially linearized counterparts of the original series that preserve an increasing degree of the underlying nonlinear structure in the original data, while randomizing the rest. This allows us to discern the difference in the manner in which the nonlinear asymmetry is expressed in the temporal and spatial data series. Comparison in the real and phase space of the original and surrogate series is performed, and the analysis reveals that the complexity of both spatial and temporal series increases with discharge and that the nature of nonlinearity is quantitatively and qualitatively different. For the spatial series, asymmetry is expressed at large scales and is shown to result from the organization of intermediate scale features. In contrast, asymmetry in the temporal series is a smaller-scale phenomenon. This is a consequence of the scale-dependent propagating velocity of topographic features. Our results have implications for understanding the complexity of geomorphic processes as a function of the space and time scale considered: the complexity over the "bed form Lagrangian time scale" is different in nature to that over the "flow velocity Lagrangian time scale".

1. Introduction

The complex organization of turbulent flow structures in the near-wall region [*Adrian et al.*, 2000; *Wu and Christensen*, 2010] makes any investigation of processes such as sediment transport complex. As such, detailed experimental [*Hardy et al.*, 2009], numerical [*Kirkil and Constantinescu*, 2010], or combined [*van Balen et al.*, 2010] studies are often needed merely to resolve the flow field, and it is only relatively recently that numerical studies have been able to couple eddy-resolving numerical methods with sediment transport models [*Zedler and Street*, 2001; *Escauriaza and Sotiropoulos*, 2011] or detailed particle imaging velocimetry work has been coupled to moving particles [*Lelouvetel et al.*, 2009].

All of this work is of increasing sophistication, but there are still significant experimental or numerical difficulties in working directly with a fully mobile bed and there is still much to be learnt about the coupled dynamics of flow and sediment motion, particularly relating to issues of the size distribution of sediment and bed armoring [*Wilcock et al.*, 2001; *Parker and Toro-Escobar*, 2002; *Blom et al.*, 2006], the dynamics of sediment patches [*Paola and Seal*, 1995; *Nelson et al.*, 2009], the manner in which flow structures preferentially entrain sediment [*Lelouvetel et al.*, 2009], and the coupled dynamics of flow, sediment, and bed forms [*Roy et al.*, 2004; *Best*, 2005; *Venditti and Bennett*, 2000; *Singh et al.*, 2011, 2012; *Keylock et al.*, 2013].

It is only relatively recently that techniques from nonlinear physics have been used to elucidate some of this complex structure. Initially, that work focussed on characterizing river beds in terms of a fractal dimension or Hurst exponent [*Nikora et al.*, 1998; *Butler et al.*, 2001; *Nikora and Walsh*, 2004]. More recently, *Singh et al.* [2009b] studied time series of bed elevation data and were able to show that as discharge increased, the nonlinearity of the bed elevation series also increased. Their study showed that the low discharge case induced a bed shear stress slightly greater than critical so that the bed was mobile but transport was

coupled to spatial or temporal stress enhancements owing to local bed topography or the action of turbulent structures. This gave dynamics that were similar to that of a diffusion process that were indistinguishable from linear variants of the original signal. Conversely, in the high discharge case, the presence of bed variability at a variety of scales from bed forms to the grain scale resulted in series with stronger nonlinearity. The three dimensionality of these features also decreased predictability through the flow–sediment–bed form coupling [*Parsons et al.*, 2005; *Venditti*, 2007]. These results were further supported by the investigations of *Singh et al.* [2011], who examined bed elevation time series as well as sediment transport rates and found that the nature of the multiscale dynamics of the bed elevation time series was controlled by flow rate and bed sediment composition.

In order to characterize the complexity of gravel bed topography, the study by *Singh et al.* [2009b] made use of finite size Lyapunov exponents (FSLEs) [*Aurell et al.*, 1996], combined with surrogate data methods [*Theiler et al.*, 1992; *Schreiber and Schmitz*, 1996] and a transport distance metric [*Moeckel and Murray*, 1997; *Basu and Foufoula-Georgiou*, 2002; *Keylock*, 2007b] to characterize the distance between the original and linearized (surrogate) time series and, thus, their degree of dissimilarity (complexity). The key departure of this present study from previous work is the use of a relatively new technique called gradual wavelet reconstruction (GWR) to probe the structure of the time and space series of bed elevations as a function of discharge. We show how this allows us to explain the important role of scale-to-scale coupling in the development of bed morphology. We make use of four different discharges and also examine the bed elevation series in two reference frames: a spatial transect extracted at the end of the experiment and a time series monitored as the bed forms were advected beneath a sonar transducer. While the former is the more commonly collected data set, and modern technology means that high-quality digital elevation models can be obtained in the field and used to make inferences about dynamic processes [*Parsons et al.*, 2007], the latter is more relevant for understanding the nature of the forcing experienced by a hypothetical "packet" of bed material as it is advected downstream in a Lagrangian fashion. Hence, differences in the nature of these types of data have implications for the best frame of reference for analyzing bed elevation data. In addition, variation in elevation characteristics as a function of discharge provides information on changes in the coupling between flow, sediment, and bed forms, while our results on the interaction between spatial scales may be linked to recent research on the importance of bed form superposition for bed form morphology [*Reesink and Bridge*, 2007, 2009] and flow resistance [*Lefebvre et al.*, 2011].

When we undertook this research, we implemented several different metrics of nonlinearity to probe into various aspects of the nonlinear structure of the bed elevation data series. These included finite size Lyapunov exponents or FSLEs [*Singh et al.*, 2009b], a nonlinear prediction error [*Schreiber and Schmitz*, 1997] and measures of the asymmetric nature of bed elevation fluctuations. However, in this manuscript we focus on the latter as they proved to be a more relevant descriptor of the form of nonlinearity than the other metrics. Hence, in the remainder of this paper, the investigation of nonlinearity is synonymous with an analysis of the asymmetry series, defined as the magnitude of the first derivative of the signal over a separation distance, Δ, raised to the third power. This is the terminology used in nonlinear physics [*Schreiber and Schmitz*, 1997], although the increment skewness, or derivative skewness, is more common in turbulence science. Our definition of complexity is then based on how similar synthetic data need to be to the original data so that metrics characterizing the asymmetry exhibit no significant difference between the original and synthetic cases.

As noted above, the main novelty of this study is the use of gradual wavelet reconstruction to develop detailed understanding of the nature of complexity and nonlinearity of the space-time series. Conventionally, surrogate data methods are used for testing the null hypothesis that there is no significant difference between data and surrogates with respect to some metric of nonlinearity. *Singh et al.* [2009b] were able to reject the null hypothesis for their high discharge case but accept it for the low discharge experiment. In this study, we use surrogate data to investigate how complex a data series is, rather than focusing on the acceptance or rejection of a null hypothesis. In the next section of this paper, we explain the technique, before describing the metrics used to compute the nonlinearity of the data series in both the real (space or time) and phase space (embedded series) domains. We then describe our experiments before presenting our results and interpreting them with respect to the proportion of energy (hence, implicitly, the number of scales) in the original signal that needs to be "fixed" in place so that the surrogate data resemble the original data in terms of our measure of nonlinearity.

2. Surrogate Data Methods and Gradual Wavelet Reconstruction

The philosophy behind surrogate data methods is to test for the presence of nonlinearity by comparing the original series with properly constructed, linearized series (called surrogates). This comparison can be done using different metrics in both the real (space or time) and phase space domains. Since the surrogates preserve linear properties of the original data, namely, the values of the data and the Fourier amplitude spectrum (hence the autocorrelative properties from the Wiener-Khintchine theorem), a significant difference in the metric computed from the data and surrogates reflects a nonlinearity in the original data with respect to the chosen metric [*Theiler et al.*, 1992]. For a chosen significance level, α and assuming a two-tailed statistical test, we generate $(2/\alpha) - 1$ surrogates and compare their values for the metric to that for the original data. A significant difference arises if the value for the original data is higher or lower than that for the surrogates.

In the next subsection we present a well-known method to generate such surrogates. We then explain how one can go beyond this to generate constrained realizations of an original time series (the surrogate data) in order to determine how similar to the original data the surrogates need to be for a significant difference to disappear. That is, how nonlinear are the data? From this we can then infer which scales and interactions mostly contribute to this nonlinearity.

2.1. The Iterated, Amplitude Adjusted, Fourier Transform Method

The original surrogate generation method of *Theiler et al.* [1992] was enhanced by *Schreiber and Schmitz* [1996] to give the Iterated, Amplitude Adjusted, Fourier Transform (IAAFT) method. Subsequently, these surrogate data techniques have seen application in a great many disciplines including the study of environmental turbulence processes [*Basu et al.*, 2007; *Poggi et al.*, 2004; *Keylock*, 2009]. They provide a null hypothesis for the behavior of linear series, to which the properties of actual time series may be compared. The IAAFT method commences with a Fourier transform of a discretely and regularly sampled data series, $h_0(x)$, with sampling interval, Δ_x:

$$H_0(f) \equiv F\{h_0(x)\} = \sum_{n=1}^{N} h_0(x) \exp[2\pi i f_n \Delta_x] = A_0(f) \exp[i\phi_0(f)] \tag{1}$$

The original amplitudes, $A_0(f)$, are stored and the original phases, $\phi(f)_0$, are replaced with the phases from a random sort of the data, $\phi_{rand}(f)$. The inverse Fourier transform is then taken and a rank-order matching procedure used to substitute the new values for original values in $h_0(x)$ to give $h_1(x)$. Hence, the histograms for $h_0(x)$ and $h_1(x)$ are identical, but the position of particular values will have changed owing to the phase randomization. However, this substitution of the original values will have decreased the accuracy of the Fourier amplitude spectrum. Hence, having obtained $A_1(f) \exp[i\phi_1(f)]$ by taking the Fourier transform of $h_1(x)$, we take the inverse Fourier transform of $A_0(f) \exp[i\phi_1(f)]$ and impose the rank-order matching to obtain $h_2(x)$. These stages are iterated until a convergence criterion is satisfied, with the amplitudes in $A_0(f)$ combined with $\phi_i(f)$, the inverse Fourier transform and rank-order matching giving $h_i(x)$.

2.2. Gradual Wavelet Reconstruction

Gradual wavelet reconstruction (GWR) [*Keylock*, 2010] uses a control parameter, $\rho \in \{0, \ldots, 1\}$, to vary the nature of the surrogate series in a systematic fashion from a linear IAAFT surrogate series ($\rho = 0$) through to the original data series ($\rho = 1$). Therefore, ρ is the proportion of energy in the original data series, fixed into the surrogate series. This technique has seen application in various ways. For example, *Keylock* [2012] studied the asymmetry (defined below) of 107 daily river discharge time series (with separation distance, $\Delta \in \{1, 7, 90\}$ days chosen to characterize various scales of behavior from daily to subannual). A choice of $\rho = 0.6$ was sufficient to preserve temporal asymmetry in all but 14 of 321 possible cases (107 data sets and three choices for Δ), while linearity was rejected using IAAFT surrogates in all but 19 of 107 rivers for at least one of the three choices of Δ. Alternatively, in an application to large-eddy simulation of flow over a wall-mounted square rib, *Keylock et al.* [2011] showed that inlet conditions randomized according to $\rho = 0.65$ could still give good results for the pressure on the front face of the rib but that $\rho = 0.90$ was needed to get the pressure on the top of the rib approximately correct owing to the importance of flow structures generated from the leading edge of the rib. Gradual wavelet reconstruction is explained in some detail by *Keylock* [2010, 2012], but we briefly review the main principles here.

GWR makes use of a time/space-frequency decomposition of a data series using wavelets. We adopt the Maximal Overlap Discrete Wavelet Transform [*Percival and Walden*, 2000], which like the continuous wavelet

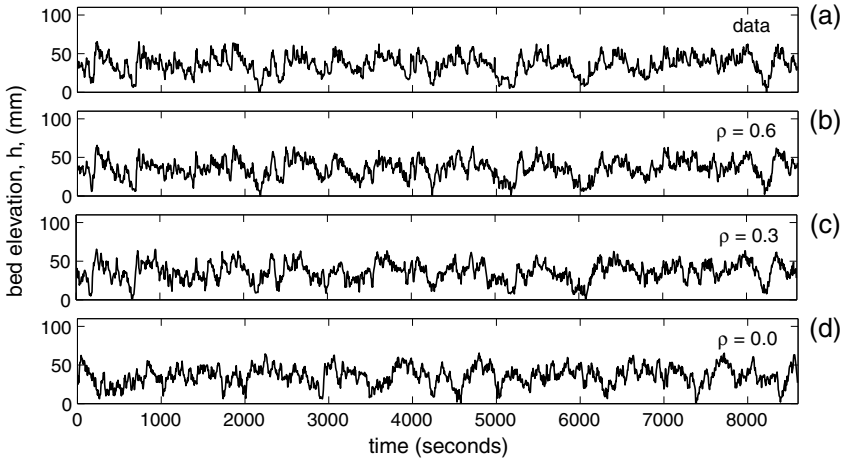

Figure 1. (a) Bed elevation time series for the Q_{800} discharge together with surrogate series for three choices of the control parameter (energy threshold), ρ. As $\rho \rightarrow 1$, the surrogate series tend to the original data. Surrogate data at $\rho = 0.0$ are produced using the IAAFT algorithm of *Schreiber and Schmitz* [1996], while data at other choices for ρ are built using the algorithm of *Keylock* [2010].

transform generates the same number of coefficients at each scale (it is undecimated) but like a discrete wavelet transform is obtained from a hierarchical bank of detail and approximation filters, retaining an exact reconstruction property. Other advantages of this choice of transform are explained by *Keylock* [2010, 2012].

Following *Keylock* [2007a], we define an energy criterion with respect to the squared wavelet coefficients, $w^2_{j,k}$, as a function of position, k, and wavelet scale (frequency band), j. The variance of the $w_{j,k}$ at a scale j is proportional to the Fourier energy at a frequency band corresponding to j. Hence, each $w^2_{j,k}$ represents the local energy content of the signal as a function of space and time, and the total energy of the signal over the set of scales considered is

$$E = \sum_{j=1}^{J} \sum_{k=1}^{N} w^2_{j,k} \tag{2}$$

In GWR, we place all $J \times N$ coefficients, $w^2_{j,k}$, in descending rank order and define the fixed coefficients as the fewest number whose total energy is greater than or equal to $\rho \times E$, where ρ is a user-selected value for the proportion of the total wavelet energy fixed in place. For $\rho = 0$, there are no fixed coefficients and the resulting surrogates are similar to those for the IAAFT. For $\rho = 1$, all coefficients are fixed, no randomization occurs, and the surrogates and data are identical. For other choice of ρ, we look at each scale in turn, place the fixed coefficients in their original positions on the time frequency plane, while the unfixed coefficients at this scale are randomized based on the methods originally developed by *Keylock* [2006, 2007a].

An example application of the method is shown in Figure 1. The data are the gravel bed topography time series, $h(x)$, obtained under a discharge of $Q_{800} = 800$ l s^{-1} as explained in detail in section 4. It is clear that as ρ increases, the surrogates take on board an increasing proportion of the temporal structure of the original series. Figure 2 shows that there is no difference in the values in these time series and that differences in the Fourier amplitude spectra only exist at the level of the convergence criterion in the underpinning algorithm. Note the slight difference in the IAAFT surrogate (gray line) at low frequencies which is due to the sensitivity of spectral methods to drift in the original signal. As noted by *Keylock* [2008], this problem can be improved by substituting the IAAFT for the wavelet algorithm presented here with $\rho = 0.0$.

2.3. Complexity Defined Using GWR

With a set of surrogates defined at various ρ ranging from 0 to 1, it is possible to define the complexity of a data series in terms of a threshold value for ρ above which there is statistically no significant difference between the original data and the synthetic surrogates at a given significance level. Thus, if $\rho_{\text{thresh}} = 0$, the original data are linear as their properties may be replicated by linear synthetic series. If ρ_{thresh} for one data series is higher than for another, then the former is defined to be more complex, irrespective of the absolute values for the metric used to characterize the intermittency. This is how GWR extends the capability of standard surrogate-based hypothesis testing in nonlinear physics and geophysics [*Theiler et al.*, 1992; *Schreiber*

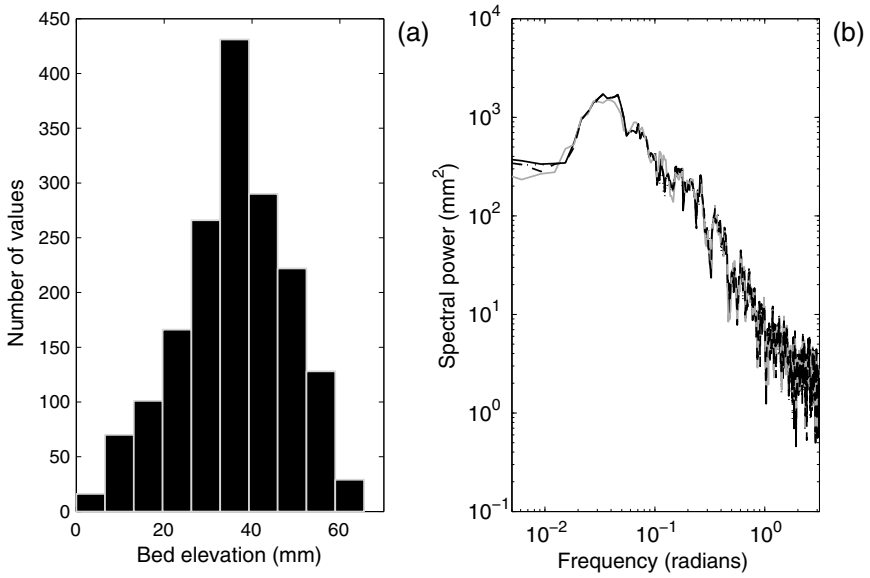

Figure 2. (a) Bed elevation histograms for the original data and the three surrogate series shown in Figure 1. The histograms are identical. (b) Fourier power spectra where the solid black line are the original data, the dashed line is for $\rho = 0.6$, the dotted black line is for $\rho = 0.3$, and the gray line is for $\rho = 0.0$.

and Schmitz, 1996]. Such methods evaluate the null hypothesis of no significant difference between an original data series and linear surrogate data (i.e., $\rho = 0$). Gradual wavelet reconstruction goes beyond this and allows us to say, given a rejection of this null hypothesis, at which ρ (i.e., ρ_{thresh}) does no significant difference any longer occur. Hence, given two nonlinear data series, traditional hypothesis testing would merely say that the null hypothesis of linearity is rejected for both. GWR allows us to see which is more complex based on the higher value for ρ_{thresh}.

3. Methods for Characterizing Nonlinearity in Gravel Bed Elevation Data

A review of various methods for characterizing the nonlinearity of time series, or spatial transect data, is provided by *Schreiber and Schmitz* [1997]. Initially, we adopted three distinct methods: temporal (or spatial) asymmetry (derivative skewness), finite time or finite size Lyapunov exponents (FSLEs), and nonlinear prediction error. Here, we focus on the former, which is directly related to the geometry of the bed forms, and therefore has a clear physical interpretation.

3.1. The Asymmetry Series $M_A(x)$

Asymmetry characterizes the skewness of the first derivative of a signal over a separation distance, Δ. Consequently, it is of use for noting departure from a linear, autocorrelative series, which can not have the "sawtooth" nature of a highly asymmetric series. This metric is useful for river discharge data sets, where the asymmetry arises from a steep rising limb relative to the falling limb [*Keylock*, 2012] and is also intimately related to fundamental principles in turbulence analysis [*von Kárman and Howarth*, 1938; *Kolmogorov*, 1941]. It is also of direct relevance to the study of bed forms where geometric asymmetry also typically exists [*Best and Bridge*, 1992; *Barnard et al.*, 2011; *Singh et al.*, 2012], and curvature near the crest plays a significant part in the dynamics of flow separation [*Venditti*, 2007].

Given a data series of bed elevations, h_x, and a choice of separation, Δ, the increment series $(h_x - h_{x+\Delta})$ is formed and its magnitude is raised to the third power to form the asymmetry series

$$M_A(x, \Delta) = |h_x - h_{x+\Delta}|^3 \tag{3}$$

In this study, and following normal practice in nonlinear analysis [*Schreiber and Schmitz*, 1997], we set $\Delta = 1$, which corresponds to 10 mm for the spatial data and 5 s for the time series data. We then drop Δ from the notation so that $M_A(x) \equiv M_A(x, \Delta = 1)$. To illustrate this, we show example spatial series of h_x and $M_A(x)$ for both the original series at Q_{800} and surrogate series for two values of ρ in Figure 3. To clarify, GWR is applied to the series h_x to create ρ surrogates and then $M_A(x)$ is calculated (equation (3)) for each of these series.

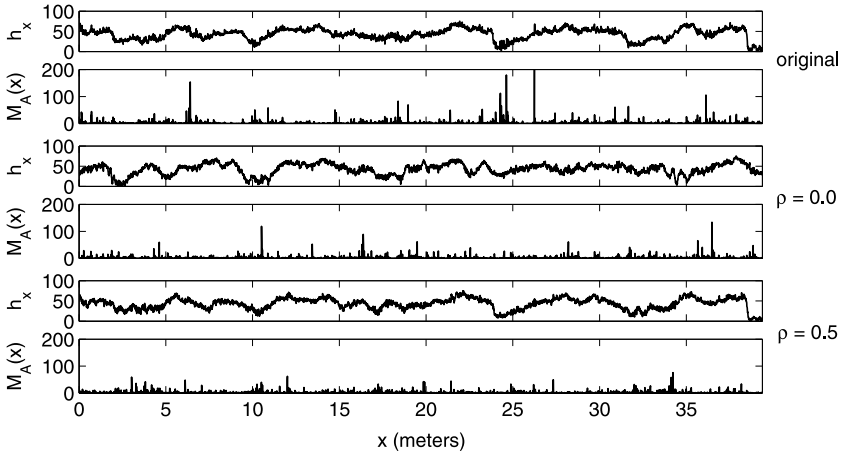

Figure 3. Bed elevation spatial series, h_x (mm), for Q_{800}, together with the derived series for $M_A(x)$ (mm^3) for the original data and $\rho \in \{0.0, 0.5\}$.

The phase randomization for $\rho = 0$ means that the major peaks and troughs in the h_x series are not aligned with those in the original data, while they are to a much greater extent for $\rho = 0.5$. However, at $\rho = 0.0$, maxima for $M_A(x)$ are closer to those for the original data than is the case for $\rho = 0.5$. This intriguing result is explored more fully below.

The summary statistic formed from the $M_A(x)$ series is the dimensionless increment skewness (the normalized third moment of the magnitude of the increment series):

$$M_A \equiv M_A(\Delta = 1) = \left\langle |h_x - h_{x+1}|^3 \right\rangle / \left\langle |h_x - h_{x+1}|^2 \right\rangle^{\frac{3}{2}} \quad (4)$$

where the angled braces indicate an ensemble average. We work with M_A and $M_A(x)$ in different ways. The former is a summary metric meaning we can compare the values for the original data and for the surrogates (as a function of ρ) in the conventional manner as explained at the start of section 2 [*Schreiber and Schmitz*, 1997]. However, in order to investigate any significance in the structure of the data series, we also compare the surrogate and original data series, $M_A(x)$. To do this, we embed them in a higher-dimensional space where their dynamics can be unfolded [*Takens*, 1981]. Hence, using subscripts 1 and 2 to indicate two different data series (e.g., this could be the original data series and a particular synthetic series), we take $M_A(x)_1$, and $M_A(x)_2$ and for an embedding dimension, m_D, and delay, τ_D, produce the embedded series, $\overrightarrow{M_1}$ and $\overrightarrow{M_2}$. For example,

$$\overrightarrow{M_1} = [M_A(x)_1, M_A(x + \tau_D)_1, \ldots M_A(x + (m_D - 1)\tau_D)_1]. \quad (5)$$

where, in this study, we adopt the values of $m_D = 3$ and $\tau_D = 10$, following the analysis of *Singh et al.* [2009b], and based on mutual information and false nearest neighbors methods, respectively [*Kantz and Schreiber*, 1997]. We then calculate the transportation distance, D_T, between $\overrightarrow{M_1}$ and $\overrightarrow{M_2}$ as explained in the appendix [*Moeckel and Murray*, 1997]. This provides a formal means for testing the difference in time series of model output and data [*Basu and Foufoula-Georgiou*, 2002]. We extend this latter approach to using GWR surrogates that are a function of the threshold, ρ.

3.2. Testing for Nonlinearity With D_T and Surrogate Data

Surrogate data methods were combined with the D_T by *Basu and Foufoula-Georgiou* [2002] and *Keylock* [2007b] for detecting nonlinearity or chaos in time series. Here we follow the method of *Basu and Foufoula–Georgiou* [2002]. We form two sets of values for D_T: first, $\mathbf{V}_1$ contains the values for D_T between the original data and each of the surrogates; second, $\mathbf{V}_2$ between each pairwise combination of the surrogate series. Thus, with a significance level, α, we have $(2/\alpha) - 1$ values in the former case and $\nabla[(2/\alpha) - 2]$ values in the latter case, where $\nabla[\ldots]$ is a triangular number. Hence, with 39 surrogates, we have 39 values in $\mathbf{V}_1$ and 741 values in $\mathbf{V}_2$. As is discussed below, the distribution functions for these sets are not necessarily normal. Thus, we evaluate the absolute difference between their median values in the results presented below.

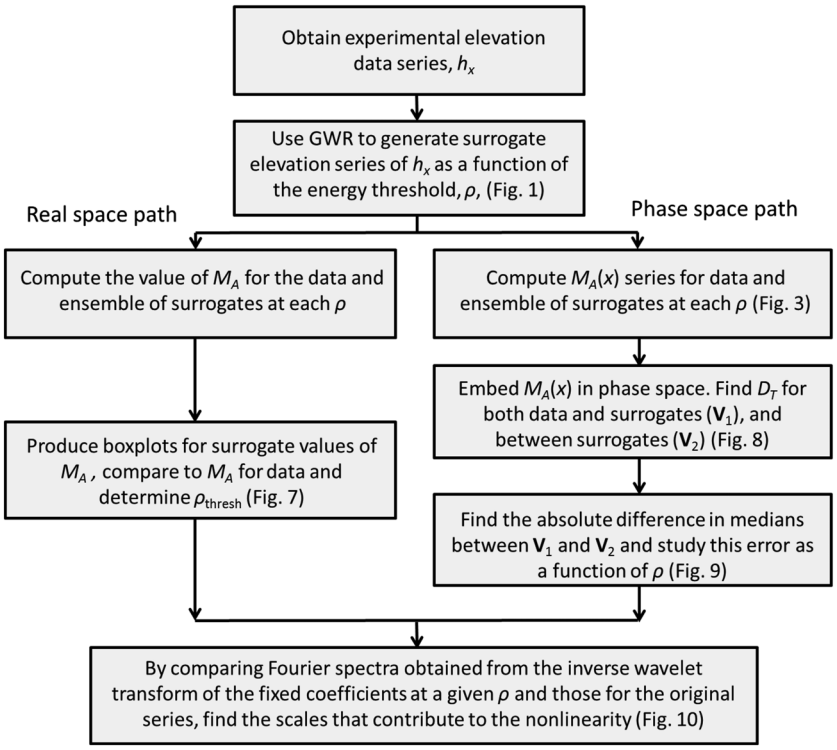

Figure 4. A flowchart explaining the analysis procedure followed in this study for comparison in real space (left path) and phase space (right path).

Figure 4 summarizes the methodology for the work that forms the focus of this paper. Surrogate data are derived from the experimental elevation series and then the metric M_A is produced for data and surrogates and compared. In addition, the series $M_A(x)$ is computed for both the original series and the surrogates, unwrapped in phase space and then the transportation distance evaluated for data to surrogates and surrogates to surrogates, before a final comparison based on the median values of the resulting distribution functions.

4. Experimental Information

4.1. Experimental Facility

Experiments were conducted in the Main Channel facility at St. Anthony Falls Laboratory, University of Minnesota. This has a 55 m long, 2.75 m wide working section, with a maximum depth of 1.8 m and maximum discharge capacity of 8000 l s^{-1}. Water discharge was controlled by a sluice gate positioned at the head end of the facility, while flow depth was regulated by a sharp-crested weir at the downstream end of the channel. While the water flows through the channel without recirculation, the sediment recirculation system is capable of entraining and recirculating particles up to 76 mm in size. The recirculation system is based on weigh pans with a 62 L capacity that independently release sediment by a tipping bucket mechanism. A horizontal, rotating auger, driven by a variable speed motor, spans the full width of the channel. When a weigh pan reaches a user-defined capacity, it tips and the auger conveys the sediment to the recirculation pump (dredging pump) intake. For more detail on this system, please see *Singh et al.* [2009a, 2010].

4.2. Grain Size and Bed Characteristics

The bed of the channel was composed of a mixture of gravel (median particle size diameter of 11.3 mm) and sand (median particle size diameter of 1 mm) in an 85:15 percentage ratio. The final grain size distribution obtained after mixing the sediments had a $d_{50} = 7.7$ mm, $d_{16} = 2.2$ mm, and $d_{84} = 21.2$ mm. The mean specific density of sediment of all size fractions was 2.65. The thickness of the bed at the start of the experiment was approximately 0.45 m.

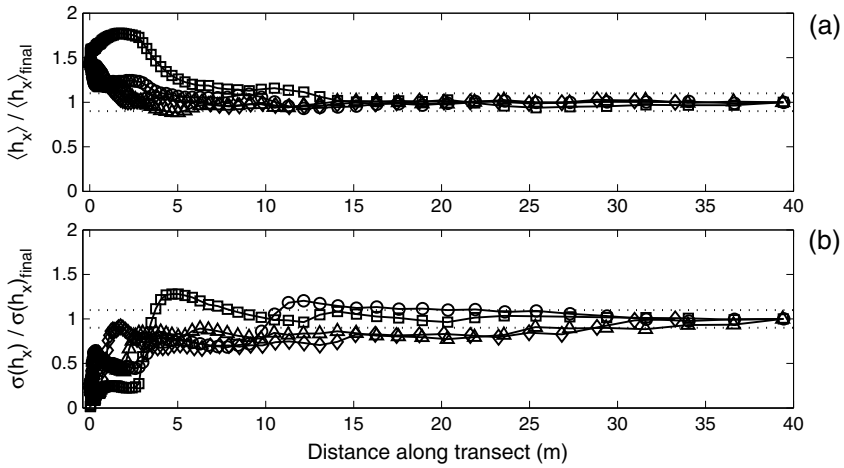

Figure 5. Convergence of the (a) mean and (b) standard deviation of the original spatial data series toward the final value. The circles, triangles, diamonds, and squares correspond to data for Q_{600}, Q_{800}, Q_{950}, and Q_{1600}, respectively. Dotted lines indicate ±10% of the final value.

The recirculation auger speed was adjusted manually every half hour to maintain a constant elevation of sediment in the auger hopper and to continuously transport sediment through the recirculation pipe. This procedure avoided sending large pulses of sediment through the pipe each time a weigh pan tipped.

4.3. Experimental Procedure

Intake of the water in the channel was directly from the Mississippi River. Prior to data collection, a constant water discharge, Q, was fed into the channel to achieve quasi-dynamic equilibrium in transport and slope adjustment for both water surface and bed. Sediment transport rates were measured simultaneously during the entire course of the run. Determination of the dynamic equilibrium state was evaluated by checking the stability of the 60 min average total sediment flux at the downstream end of the test section. Using the pan accumulation data, the acquisition software computed a 60 min mean of sediment flux in all five pans. Dynamic equilibrium was reached when the average of the previous 60 min of instantaneous flux values computed from the pan data stabilized. After attaining equilibrium, experiments ran for approximately 5 h. The convergence of the mean and standard deviation for the bed form elevation data is shown in Figure 5. The mean (Figure 5a) has converged to within 10% of its final value for all discharges by less than half way along the channel, while the standard deviation (Figure 5b) has converged by three quarters of the way along. Hence, there is evidence that these experiments are statistically repeatable.

Time series of bed elevations were measured through four stationary submersible sonar transducers of 2.5 cm diameter, mounted at the end of rigid steel tubes with a diameter 1.5 cm. The transducers were placed approximately 0.17 m above the mean bed elevation, were directed perpendicular to the bed, and were fully submersed for all experiments. Three sonars were located 1.23 m upstream of the five weigh pans used to collect and weigh the transported sediment (see Figure 6). Data from the central one of these (labeled h_x in Figure 6) were used in this study. Sonar data were sampled every 5 s with a vertical precision of 0.1 mm. The spatial transects were obtained at the end of the experiments over a drained bed. A range-finding laser (vertical precision of 0.1 mm and horizontal of 1 mm) was mounted on a three-axis positionable data acquisition carriage that was capable of traversing the entire 55 × 2.75 m test section

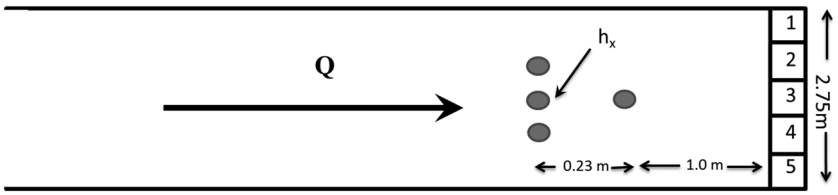

Figure 6. The location of the five weigh pans (numbered) and the four sonars (circles) at the end of the working section of the Main Channel facility. The time series data used in this study were obtained from the upstream sonar on the flume center line (labeled h_x).

Table 1. Hydraulic Properties of the Experiments[a]

Attribute	600 l s^{-1}	800 l s^{-1}	950 l s^{-1}	1600 l s^{-1}
Flow depth (m)	0.217	0.245	0.270	0.365
Flow velocity (m s^{-1})	1.01	1.19	1.28	1.59
Water surface slope	0.0050	0.0053	0.0050	0.0037
Hydraulic radius (m)	0.187	0.208	0.226	0.288
Mean bed form height (cm)	2.53	3.17	3.91	4.41
S.d. bed form height (cm)	0.67	1.26	1.55	2.34
Mean bed form length (m)	6.20	4.88	3.46	3.10
S.d. bed form length (m)	4.25	2.19	1.36	1.33
Spectral slope	−1.31	−1.67	−2.07	−2.39
Bed form propagation velocity (m h^{-1})	9.57	23.7	30.8	30.7

[a]S.d. is the standard deviation.

and could position probes to within 1 mm in all three axes. Measurements were taken every centimeter (i.e., half the D_{84}) down the channel center line for a distance of ~40 m. This resolution is, consequently, sufficient to resolve the larger grains and the topographical features that develop in the channel. Measurements were also made laterally at the same spacing, although they are not reported here. Bed elevation acquisition data were also synchronized with measurements of flow velocity, attained with a Nortek Vectrino acoustic Doppler velocimeter; tracer particle experiments were also conducted.

Four different discharges were used in the experiments reported here, and the hydraulic conditions pertaining in each case are listed in Table 1. In addition, this table states the means and standard deviations for the height and length of the bed forms, as well as the slope of the Fourier power spectral density against wavelength on logarithmic axes, indicating the scaling of bed form sizes over the range 0.1 m to 2.0 m (larger wavelengths than this correspond to the dominant bed form scale as seen in Table 1). It is clear that as the discharge increases, the mean bed form height increases and the mean bed form length decreases, indicating a significant steepening of the lee and stoss sides of the bed form. The product of these variables indicates a slight decay in volume of the bed forms with discharge. The trend for the standard deviation is greater than the mean; hence, the coefficient of variation varies in a similar manner to the means. Thus, there is no obvious change in the stability of the average morphological pattern with discharge: while length variability decreases with discharge, height variability increases. The spectral slopes are steeper at higher discharges despite the mean wavelength decreasing. This is a consequence of the decrease in the standard deviation (and coefficient of variation) of bed form length with discharge, meaning that the energy associated with the bed forms is smeared across fewer wavelengths. Thus, a steeper decay of the energy with wavelength results. More details about the extracted bed forms and associated spectral analysis will be presented in a forthcoming paper.

The bed form propagation velocities are also quoted. These are defined in terms of the motion of the points that are at least as high as the mean bed form height +2 standard deviations and permit the effective sampling resolution of the spatial and temporal sampling to be compared. The former is at a wavelength of 0.01 m. With a 5 s sampling resolution, the equivalent values for the temporal sampling are 0.013 m (Q_{600}), 0.033 m (Q_{800}), 0.043 m (Q_{950}), and 0.043 m (Q_{1600}).

5. Results

5.1. Results for M_A Asymmetry Comparison in Real Space

Figure 7 shows that there is a clear contrast in the values for M_A between the spatial and temporal data series. Figure 7 (top) shows that irrespective of discharge, the overlap between M_A for the original elevation series (dotted line) and the boxplots of M_A for the surrogates means that the spatial transects of bed elevation series do not exhibit a significantly different asymmetry to their linear counterparts for $\rho = 0.0$. Although there is no significant difference at $\rho = 0.0$, it is interesting to note that as ρ increases and we constrain the degree of variation in the surrogates, a significant difference emerges. The surrogates for Q_{1600} preserve a high degree of variation for the highest choice of ρ and, as a consequence, do not exhibit a significant difference between data and surrogates until $\rho = 0.6$, compared to $\rho = 0.2$, $\rho = 0.1$, and $\rho = 0.2$ for Q_{600}, Q_{800} and Q_{950}, respectively. Related to this is the observation that when working from the right-hand side of these plots, the value for M_A is only attained by $\rho = 0.99$ for Q_{1600}, while the equivalent values are

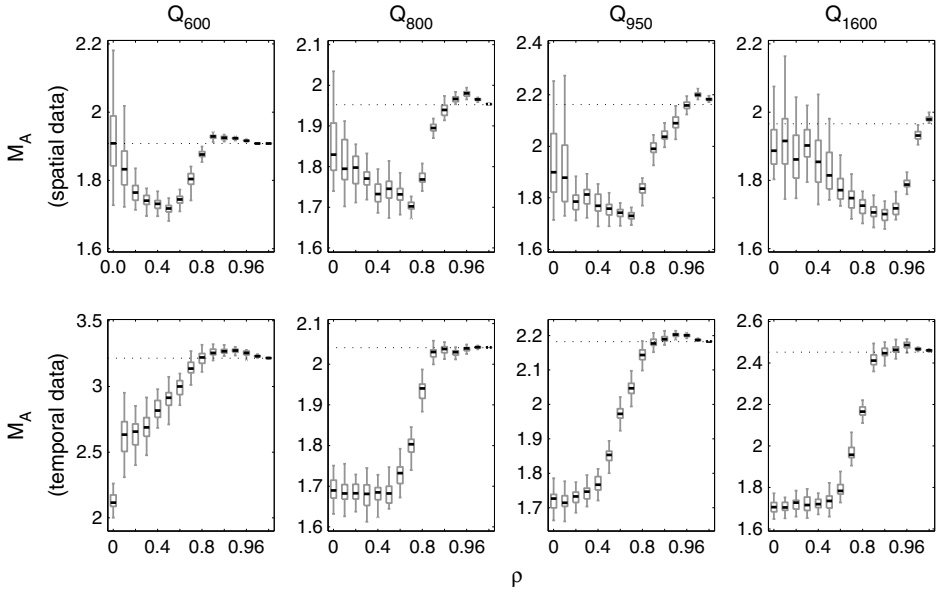

Figure 7. Results for the gradual wavelet reconstruction of the asymmetry measure, M_A, for the bed elevation data as a function of flow discharge: (top) spatial transects and (bottom) temporal series. The value of M_A for the data is shown as a dotted line, and the results for 39 surrogates are contained in the boxplots. From left to right, these are for $\rho \in \{0.0, 0.1, 0.2, 0.3, 0.4, 0.5, 0.6, 0.7, 0.8, 0.9, 0.92, 0.94, 0.96, 0.98, 0.99\}$. The line in the center of each box is the median, with the upper, q_3, and lower, q_1, quartiles delimiting the extent of the box. The whiskers then extend to $q_3 + 1.5(q_3 - q_1)$ and $q_1 - 1.5(q_3 - q_1)$. Starting from $\rho \sim 1$, the last value for ρ for which the M_A of the ρ surrogates are not significantly different to the original data defines ρ_{thresh}, e.g., $\rho_{\text{thresh}} = 0.9$ in Figure 7 (top left). The discharge dependence of these values is examined in Figure 11.

$\rho = 0.90$, $\rho = 0.92$, and $\rho = 0.96$ for Q_{600}, Q_{800}, and Q_{950}, respectively. These latter values have previously been termed the threshold values for ρ in GWR-based analyses [*Keylock*, 2012]. A data series with a high value for ρ_{thresh} may be considered more complex because a higher proportion of the temporal/spatial structure (a higher proportion of the wavelet energy of the data series) needs to be fixed in place in order for the surrogates to replicate the properties of the original data. Note that there is a discharge dependence to these values for ρ_{thresh}: as discharge increases, the series become more complex, despite the facts that the magnitude of M_A does not vary greatly.

Hence, the asymmetry behavior in the spatial transects is rather subtle. Unconstrained, linear surrogates can sample this degree of asymmetry by chance. However, when the surrogates are constrained to a shape that is more similar to those of the observed bed forms, the results support the hypothesis that the increase in discharge increases the bed form complexity.

Regarding the time series of elevations, there is a clear significant difference in asymmetry at $\rho = 0.0$ between data and surrogates for all cases. Thus, all these data series are nonlinear with respect to M_A. Working from the right-hand side of the lower row of plots in Figure 7, the values for ρ_{thresh} are 0.7 for Q_{600}, 0.9 for Q_{800}, 0.8 for Q_{950}, and 0.9 for Q_{1600}. Hence, there is perhaps a weak tendency for a discharge dependence in the time series results.

5.2. Results for $M_A(x)$ Comparison in Phase Space

We analyzed the differences in $M_A(x)$ between data and surrogates using D_T. We formed the sets $\mathbf{V}_1$ and $\mathbf{V}_2$ corresponding to the values for D_T between, first, the asymmetry series of the original data and the asymmetry series of the surrogates and, second, the asymmetry series for each surrogate series and all the others. These distributions are shown by the heavy ($\mathbf{V}_1$) and thin ($\mathbf{V}_2$) lines in Figure 8 as a function of ρ for the Q_{600} spatial data series.

The absolute difference in the medians of $\mathbf{V}_1$ and $\mathbf{V}_2$ is shown in Figure 9 as a function of discharge and ρ. The results reflect those seen in Figure 7: For the spatial data and for very low ρ, the large intrinsic variation in the surrogates results in a small difference in the medians, while for very high ρ, the surrogates are very similar to the data and the difference is also small. In between, the difference increases until the properties

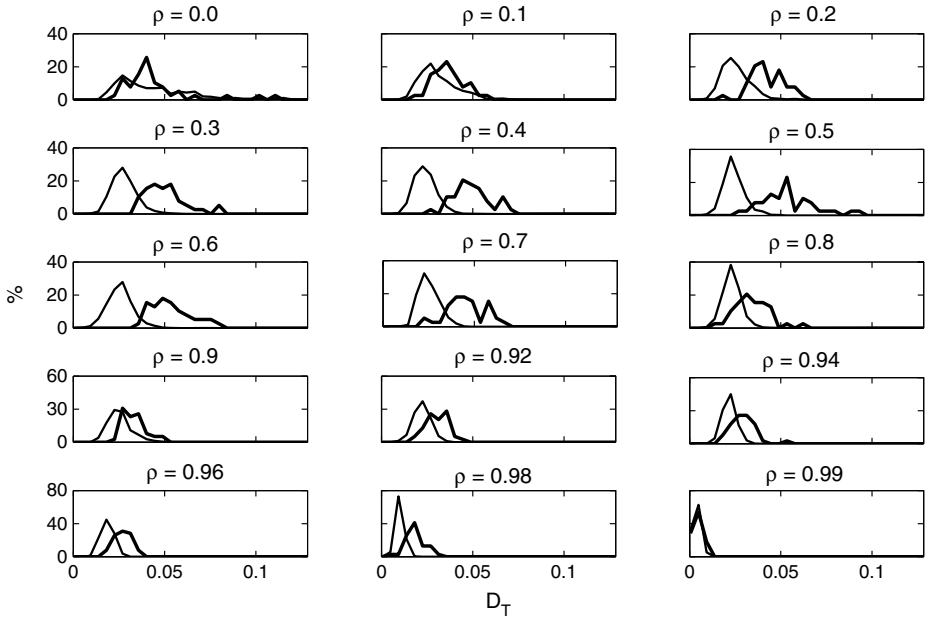

Figure 8. Results for the transportation distance, D_T, in phase space computed from the $M_A(x)$ series of the original data and their surrogates as a function of ρ for the Q_{600} spatial data series. The heavy lines indicate the histograms for the results between the data and surrogates (i.e., $\mathbf{V}_1$) and the thin lines ($\mathbf{V}_2$) indicate the intrinsic variation between surrogates. Note the small difference in the medians of these histograms for small and large ρ, with a maximum difference at $\rho = 0.5$. This pattern is summarized in Figure 9 (top left).

of the surrogates seem to "lock on" to those of the original data, at which point the difference declines. In the case of the temporal data, the pattern we see is more like the one we expected—a significant difference at $\rho = 0.0$ and either a general decrease in $|\mathbf{V}_1 - \mathbf{V}_2|$ with ρ (as is the case for Q_{600}) or an error plateau until a critical value for ρ, followed by a rapid decline (higher discharge cases). For these data, not only does the median difference at $\rho = 0$ increase with discharge but also the critical value for ρ at which significant decay in the error arises: For Q_{600}, the error decays from $\rho = 0$ (and more steeply from $\rho = 0.8$). For Q_{800} and Q_{950}, the error is stable until $\rho = 0.5$, while for Q_{1600}, the region of relative stability persists until $\rho = 0.6$.

The maximum median difference for the spatial data in Figure 9 (top) shows a peak at $\rho = 0.5$ for Q_{600}, which increases to $\rho = 0.7$ for Q_{800} and Q_{950}, and increases further to $\rho = 0.94$ for Q_{1600}. Hence, a far higher proportion of the total wavelet energy needs to be fixed in place in the surrogates to move beyond this maximum error value as discharge increases. Thus, we have an interesting and unanticipated result that reflects behavior seen in Figure 7: The difference in $M_A(x)$ complexity for the spatial data is not apparent in conventional IAAFT testing at $\rho = 0.0$ but emerges in terms of the coupling behavior of fixed and unfixed scales that requires much more energy to be fixed as discharge increases. This highlights an advantage of GWR compared to conventional surrogate data testing. From the perspective of hypothesis testing for nonlinearity, it is correct to state that for our spatial data (Figures 7 and 9) there is no significant difference between the original data and phase randomized, linear surrogates (at $\rho = 0$) and there is no significant asymmetry to the data. However, once a degree of phase locking is introduced, i.e., once some proportion of the wavelet energy of the original signal is fixed in place, significant asymmetry emerges. This can be seen in Figure 3 for the spatial series of Q_{800}. Pure phase randomization results in occasional large values for $M_A(x)$ as seen for the original data. However, at $\rho = 0.5$, where the surrogate series for h_x resembles that for the original data qualitatively, peaks in the asymmetry are greatly reduced, reflecting the difference in medians seen in Figure 9. This implies that for multiscale systems, such as bed forms where there is an interaction between form, grain, and intermediate scales, conventional formulations for surrogate data-based hypothesis testing may need rethinking.

This issue is examined further in Figure 10, which shows three Fourier power spectra (multitaper method) for each discharge obtained from the centered spatial data series. The black line in each case is obtained from the experimental data. The gray lines are derived by working out the fixed wavelet coefficients at a

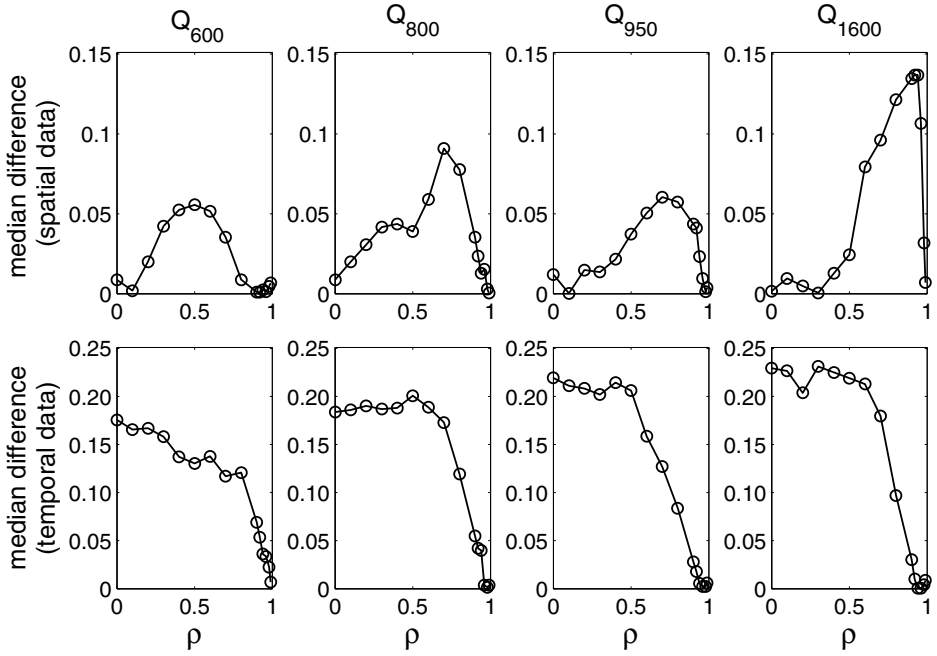

Figure 9. The unsigned difference in the median values of the histograms for $\mathbf{V}_1$ and $\mathbf{V}_2$ (see caption for Figure 8 or the text for further explanation). Values for $\mathbf{V}_1$ are obtained by computing the D_T in phase space between the original $M_A(x)$ series and the ρ surrogate series. In the case of $\mathbf{V}_2$, D_T is computed between pairwise combinations of ρ surrogate series. This method is described more fully in section 3.2. The discharge for the plots in each column is shown across the top of the figure. The top row of results are for the spatial data, with the temporal data on the bottom row. The values of ρ at which the maximum median difference is observed are called critical values, ρ_{crit}. These are used to understand the scales mostly contributing to the nonlinearity (Figure 10) and exhibiting a discharge dependence (Figure 11).

given ρ, setting all other coefficients to zero and taking the inverse wavelet transform. Hence, they represent the Fourier spectra for the spatial elevations derived from the fixed wavelet coefficients at a given ρ. The unfixed coefficients need to be added to this to obtain a spectrum that converges on the black line in each case as arises in Figure 2. The solid gray line is for the choice of ρ corresponding to the error peak in the top row of Figure 9, while the red line is for the next choice of ρ. That is, for Q_{600}, these values are for $\rho = 0.5$ and $\rho = 0.6$, respectively. When examining the solid gray lines, a strong spectral gap is evident at a frequency that increases with discharge from just less than 0.2 radians for Q_{600} to 0.5 radians for Q_{1600}. That is, the energetic wavelet coefficients fixed in the algorithm occur preferentially at low frequencies (as the shape of the spectrum in Figure 2 indicates), but also at higher frequencies, with a gap at intermediate frequencies. Increasing ρ further removes the gap. Thus, the complex error structure for $M_A(x)$ for the spatial data seen in Figures 3 and 9 is a consequence of the coupling between the intermediate scales and the low- and high-frequency scales. When ρ is small, most scales are phase randomized and $M_A(x)$ for the data can be obtained by chance. At high values for ρ, wavelet coefficients in the spectral gap become fixed (red lines in Figure 10) and the error decreases. For intermediate values for ρ, the error increases because the randomization of the coefficients preferentially located in the spectral gap in Figure 10 is sufficiently constrained to reduce the probability of an appropriate phase alignment with the fixed coefficients (Figure 3).

The spectral gap evident in the red lines in Figure 10 suggests that there is significant energy at both the small (grain) and large (bed form) scales, which correspond to classical notions of grain and form roughness [*Lawless and Robert*, 2001]. However, we have shown that in order to obtain synthetic data series with nonlinear characteristics that match those of gravel bed data series, the coupling between these scales must also be captured, via intermediate scale, superimposed bed forms. This is a new result and the manner that we have determined this, using techniques from nonlinear physics coupled to a constrained randomization technique (gradual wavelet reconstruction) is also novel. This highlights some of the potential power of using GWR to elucidate characteristics of complex earth and environmental systems.

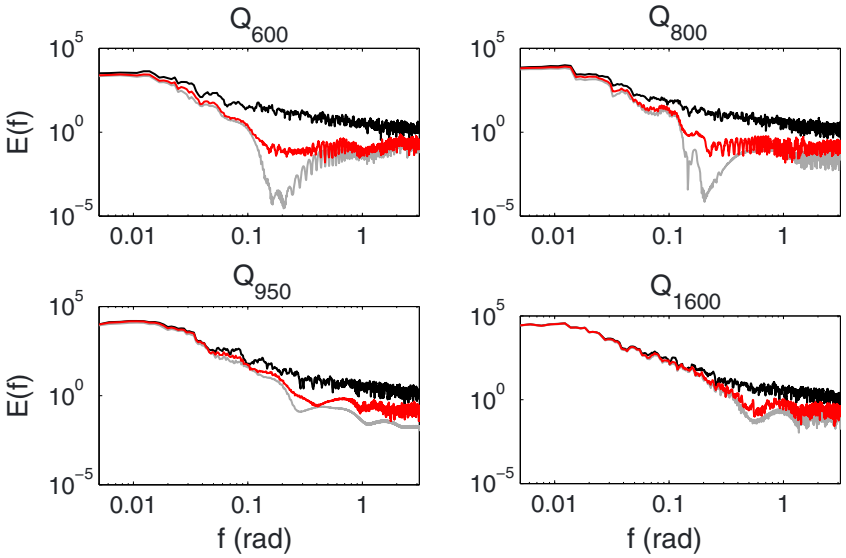

Figure 10. Fourier power spectra computed using the multitaper method for the spatial data series (black line), the series of fixed wavelet coefficients at the ρ giving the maximum median difference in the top row of Figure 9 (gray line), and the series of fixed wavelet coefficients for the next larger value for ρ (red line). The difference in spectral energy between the gray and red lines (spectral gap) indicates that the coupling of intermediate scales to the larger and smaller scales contributes substantially to the nonlinearity of the bed elevation series and that the wavelength of the coupled scales moves to higher frequencies with increasing discharge.

6. Discussion

6.1. Summary

A comparison of the discharge dependence for the asymmetry series, $M_A(x)$, in both real space and phase space is given in Figure 11. The upper panel shows the discharge dependence for ρ_{thresh} for M_A, where this threshold is the further point toward $\rho = 1$ that separates surrogates that are significantly different to the original data ($\rho \leq \rho_{\text{thresh}}$) and those that are not significantly different $\rho > \rho_{\text{thresh}}$. For both the spatial (squares) and temporal (diamonds) data, a discharge dependence is evident. Hence, as discharge increases, the asymmetry becomes more complex. Figure 11b highlights critical values for ρ for the analysis of $M_A(x)$ for the spatial data series. This definition is not equivalent to ρ_{thresh} but is the ρ corresponding to the maximum for the absolute difference in medians between $\mathbf{V}_1$ and $\mathbf{V}_2$. These ρ_{crit} values have a very clear

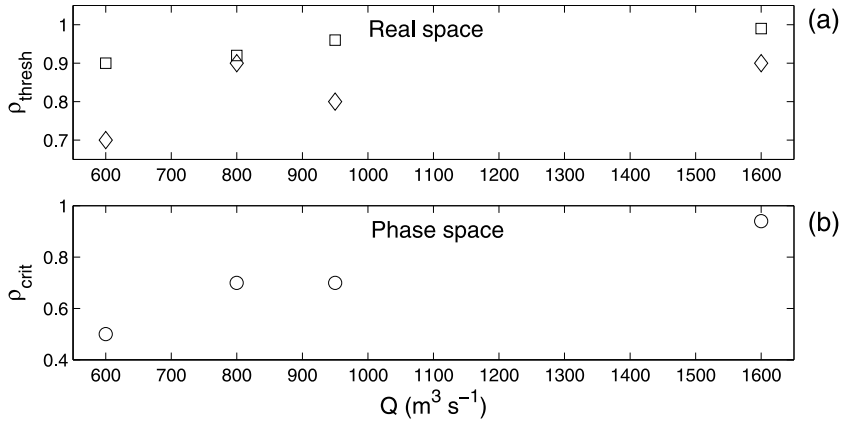

Figure 11. A summary plot of the discharge dependencies of threshold and critical values for ρ. (a) ρ_{thresh} as the last value for ρ (working from $\rho = 1$), where no significant difference between data and surrogates occurs (see Figure 7). The results for the spatial elevation series are shown as squares and the time series as diamonds. (b) the ρ_{crit} values (circles), i.e., the value of ρ at which the maximum median difference is found in the phase space between $M_A(x)$ for the original data and their ρ-surrogates (see Figure 9).

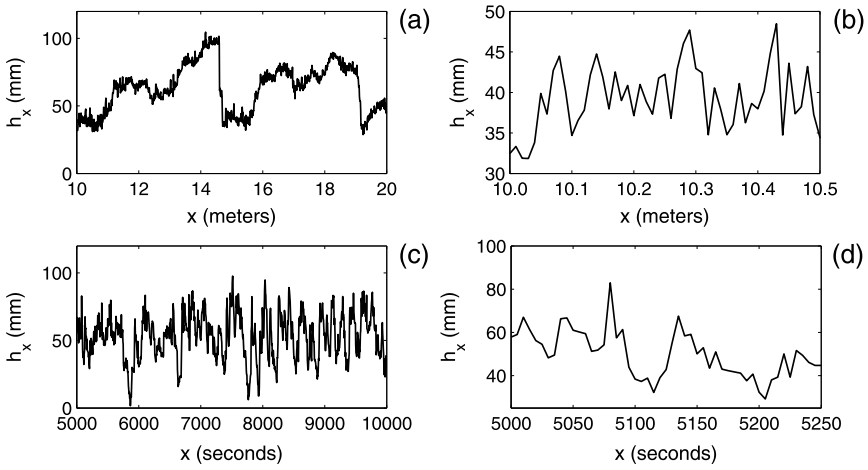

Figure 12. The elevation data series for Q_{950}. The data in (a) and (b) are the spatial transects while those in (c) and (d) are the time series. Panels (b) and (d) highlight subregions of the results shown in (a) and (c).

discharge dependence, meaning a greater proportion of the wavelet energy of the signal needs to be fixed in place for the effect examined in Figure 10 to occur.

Perhaps the most interesting result of our study, however, is not seen in Figure 11 but is in Figures 7 and 9. No significant nonlinearity would be inferred for M_A or $M_A(x)$ at $\rho = 0$. Hence, without the use of GWR, one would conclude that there is no significant asymmetry and, thus, if nonlinearity is suspected, M_A is not sufficiently sensitive to the nature of the nonlinearity to exhibit a significant difference. However, as ρ increases a significant difference emerges and the basis for this is shown in Figure 10. A spectral gap develops in the fixed coefficients with large and small scales fixed to some extent but intermediate scales randomized. However, constraints in the randomization mean that the intermediate scales are systematically displaced in phase compared to the original data or to the full phase randomization that occurs at $\rho = 0$ (Figure 3). The wavelength of these intermediate scales moves to higher frequencies as discharge increases. The dimensionless spatial frequencies in Figure 10 correspond to physical length scales of 30–40 cm (Q_{600} and Q_{800}), 25 cm (Q_{950}), and 10–12 cm (Q_{1600}). Hence, these crucial intermediate scales shorten as discharge increases, in line with the general shortening of the bed forms with discharge reported in Table 1.

6.2. Interpretation

Figure 12 shows the data series for Q_{950} where the values for M_A for both the original spatial and temporal series are similar (Figure 7). A comparison between Figures 12a and 12b shows that for the spatial data, asymmetry is a large scale phenomenon. The gradual rise and sudden fall in the bed elevations seen from $x = 12$ m to $x = 14.5$ m in Figure 12a is not reflected in the smaller scales, which have a more symmetric behavior (Figure 12b). In contrast, there is no clear asymmetry in Figure 12c at the large scales, but it becomes evident at smaller scales such as between 5100 and 5200 s in Figure 12d. Consequently, with the asymmetry/nonlinearity evident at small scales in the latter case, there is no issue regarding cross-scale coupling for the preservation of asymmetry. However, if the asymmetry is a large-scale phenomenon, the question arises as to whether it is innately a large-scale process or is a consequence of the integrated effects of smaller-scale phenomena. The results in Figure 10 imply that it is about the coupling of the intermediate scales to the grain and bed form scales.

As noted above, the wavelength of the spectral gap for Q_{950} in Figure 10 is $\sim$ 18 to 31 cm. Features corresponding to this range of wavelengths for the spatial elevation series at Q_{950} are highlighted in Figure 13. These "ridges" exert a strong control on the asymmetry despite being of lower energy than the bed forms and some of the grain-scale fluctuations. The development of gravel bed forms with a suitable asymmetry therefore concerns the coupling between the bed form and grain scales through these intermediate scale features. Hence, the error peak in Figure 9 at $\rho = 0.7$ for Q_{950} is shown in Figure 10 to correspond to features in Figure 13 that at $\rho = 0.7$ are not fixed in place in the wavelet coefficients but are crucial for generating the requisite asymmetry.

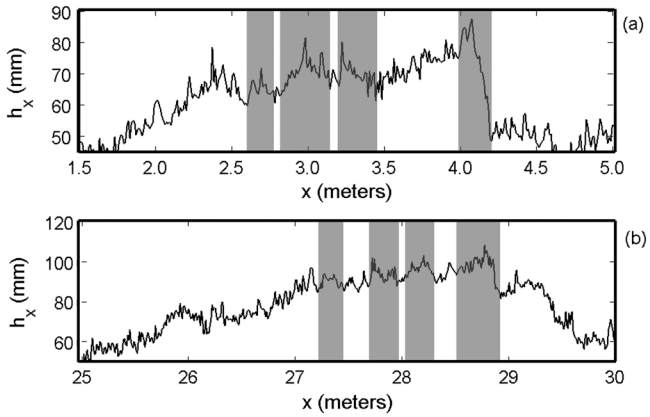

Figure 13. Two subsections of the spatial elevation data series for Q_{950}. Features with a wavelength corresponding to the spectral gap in Figure 10 are highlighted in gray.

7. Conclusion

The statistical properties of gravel bed surfaces have been the focus of concentrated research effort in the last few years [*Nikora et al.*, 1998; *Butler et al.*, 2001; *Aberle and Nikora*, 2006]. Even in the absence of fully developed bed forms such as dunes [*Best*, 2005], understanding bed roughness is important because the coupling between roughness elements on the bed, turbulence production, and flow dynamics [*Lacey and Roy*, 2007; *Hardy et al.*, 2007; *Lefebvre et al.*, 2011; *Keylock et al.*, 2013] is vital for enhancing the efficacy of flow resistance and sediment transport equations [*Simons et al.*, 1965].

The results of this study throw a different light on previous work characterizing gravel bed surfaces. The complexity of the surfaces as measured by asymmetry increases with discharge (Figure 11) and, thus, velocity (Table 1). However, the crucial difference is the manner in which the asymmetry is expressed between the spatial and temporal data, which is seen in the different shape of the plots in Figures 7 and 9 and was also seen in the analysis of finite size Lyapunov exponents (results not reported here). For the spatial elevation data series, the key role of the intermediate scales (Figures 10 and 13) in coupling large (bed form) scales and small (close to grain) scales to reproduce the asymmetry in bed elevation fluctuations is a new result. Hence, superimposed topographic features are not just important in terms of their sedimentological effects [*Smith*, 1972; *Reesink and Bridge*, 2007, 2009], impact on hydraulic roughness [*Lefebvre et al.*, 2011], or role in boundary layer turbulence processes [*Barnard et al.*, 2011] but have a role in controlling the complexity of the whole bed form unit through their impact on derivative skewness statistics.

In addition, we have determined that the time series bed elevation data are more likely to exhibit complexity with respect to IAAFT surrogates (i.e., $\rho = 0$) than spatial data series. This is because the nonlinearity appears at much smaller scales as shown in Figure 12. This observation has implications for the relevant time scales for the examination of geomorphic phenomena. At the time scale of the fluid velocity (the fluid velocity Lagrangian time scale), the bed is approximately stationary for our flow conditions (Table 1 shows that the flow velocity is at least 150 times the bed form velocity). Hence, the spatial data series is of relevance. While flow over such surfaces is clearly very complex [*Best*, 2005; *Hardy et al.*, 2007; *Venditti*, 2007; *Keylock et al.*, 2013], because the nonlinearity is expressed at larger scales, two-point statistics (i.e., second-order measures, such as the fractal geometry of the surface, [*Butler et al.*, 2001]), supplemented by knowledge of the bed elevations and directional information, are likely to be effective for the characterization of small scale roughness statistics [*Aberle and Nikora*, 2006]. The difficulty then resides with the coupling to the highly nonlinear Navier-Stokes equations, meaning that eddy-resolving flow modeling techniques have an important role to play [*Escauriaza and Sotiropoulos*, 2011; *Keylock et al.*, 2012c].

In contrast, when working at the time scale of bed evolution and migration (the bed form Lagrangian time scale, which in this study varies from $\sim$ 10 m h^{-1} to $\sim$ 30 m h^{-1}), the elevation data are complex at relatively smaller scales of variability. This difference is a consequence of the scale-dependent propagating velocity of topographic features. This raises the specter that coupling bed form dynamics to channel adjustment and evolution scales will require careful consideration of the precise nature of the bed surface properties.

This is because even though such processes are likely to be less complex than turbulence, the bed elevation data are more complex in their own right when analyzed from the perspective adopted here.

The results of any study depend on the sampling duration and resolution adopted. By measuring every centimeter for 40 m, we have high confidence in being able to identify intermediate scale topographic features and examine their coupling to larger scales. It is possible that interesting and potentially complex behavior is also present at scales smaller than those resolved here (the order of the median grain size). The sand fraction in particular is known to sometimes exhibit behavior that is qualitatively different to gravels in weakly bimodal mixtures [*Wathen et al.*, 1995]. What these effects are and how they are coupled to, and potentially mediate, the phenomena investigated here, is a question for future research.

Matlab code to perform gradual wavelet reconstruction and to calculate the transportation distance, D_T, is available for download from www.chriskeylock.net.

Appendix A: Transportation Metric

For an embedding dimension, m_D, and delay, τ_D, we produce embedded series, $\overrightarrow{M_1}$ and $\overrightarrow{M_2}$ (equation (5)). *Moeckel and Murray* [1997] then discretizes the data into b intervals. We tested two implementations to handle the positively skewed nature of $M_A(x)$: an equal interval method based on the logarithm of $M_A(x)$ and a classification where there are an equal number of points in each interval (an equal size method). The results presented in the paper use the latter.

Given a choice of b, and a selection of the equal interval or equal size approach, one obtains $\beta = b^{m_D}$ hypercubes. We can evaluate the probability of the two systems being in each hypercube by simply determining the number of points in each cube and dividing these values through by N for each series. One then minimizes the transportation cost between the two distribution functions. Thus, we define $\mu_{i,i/}$ as the amount of mass to be moved between hypercubes B_i and $B_{i/}$ and adopt the constraint

$$\sum_{i/}(\mu_{i,i/} - \mu_{i/,i}) = p(\overrightarrow{M_1})_i - p(\overrightarrow{M_2})_i \tag{A1}$$

where $i = 1, \ldots, \beta$ and the sum is over the immediate neighbors of B_i. If $\mathbf{T}[p(\overrightarrow{M_1}), p(\overrightarrow{M_2})]$ is the set of all the transportation routes that fulfill (A1), then we seek the minimum from this set:

$$D_T[p(\overrightarrow{M_1}), p(\overrightarrow{M_2})] = \inf_{\mu \in \mathbf{T}[p(\overrightarrow{M_1}), p(\overrightarrow{M_2})]} \sum_{i,i/=1}^{\beta} \mu_{i,i/} D_M(B_i, B_{i/}) \tag{A2}$$

where $D_M(B_i, B_{i/})$ is a normalized Mahalanobis distance:

$$D_M(B_i, B_{i/}) = \frac{1}{m_D} \sum_{i=0}^{m_D - 1} |B_{i_i'} - B_{i_i}| \tag{A3}$$

Notation

A	Fourier amplitudes.
α	significance level.
b	number of subdivisions of an axis of an embedding space.
B	a particular hypercube within the embedding space.
β	total number of hypercubes in an embedding space.
γ, ξ	subscripts for two different data vectors.
d_{16}, d_{50}, d_{84}	sediment size percentage fractions based on diameter.
D_M	Mahalanobis distance.
D_1	distance metric.
D_T	transportation distance metric.
Δ	separation of two points along a data series.
Δ_x	sampling interval of a data series.
E	energy measure in terms of wavelet coefficients.

$E(f)$ Fourier energy spectrum.
f frequency.
h data series (space or time) of bed elevation heights (mm).
H Fourier transform of h.
i imaginary part or as an index variable for the boxes in a discretized embedding.
I_M mutual information.
j wavelet scale.
J maximum wavelet scale.
k position along a set of wavelet coefficients at a given scale, j.
m_D embedding dimension.
M_A metric for data asymmetry in real space (increment skewness).
$M_A(x)$ Asymmetry data series subsequently analyzed in phase space.
$\vec{M}$ embedding vector for asymmetry data series, $M_A(x)$.
μ amount of probability "mass" to be moved between boxes in a discretized embedding.
N number of points in a data series.
$\nabla[\ldots]$ triangular number.
p probability.
ϕ Fourier phases.
q quartile.
Q discharge.
ρ parameter for gradual wavelet reconstruction.
σ standard deviation.
$\mathbf{T}$ set of transportation plans.
τ_D delay time for a state space embedding.
τ_{h*} time scale for data series, h, based on autocorrelation.
$\tau_{\hat{h}}$ time scale for data series, h, based on mutual information.
$\mathbf{V}_1, \mathbf{V}_2$ Sets of values for D_T between data and surrogates, and surrogates and surrogates, respectively.
w wavelet coefficient.
x position along a data series (space or time).
z normalized data in terms of z scores.

Acknowledgments
AS and EFG acknowledge support by NCED (award EAR-0120914) and by NSF grants EAR-0824084 and EAR-0835789. We are grateful to the Associate Editor and reviewers for their comments, which resulted in various improvements to this manuscript.

References

Aberle, J., and V. Nikora (2006), Statistical properties of armored gravel bed surfaces, *Water Resour. Res.*, *42*, W11414, doi:10.1029/2005WR004674.
Adrian, R. J., C. D. Meinhart, and C. D. Tomkins (2000), Vortex organization in the outer region of the turbulent boundary layer, *J. Fluid Mech.*, *422*, 1–54.
Aurell, E., G. Boffetta, A. Crisanti, G. Paladin, and A. Vulpiani (1996), Predictability in systems with many characteristic times: The case of turbulence, *Phys. Rev. E*, *53*, 2337–2349.
Barnard, P. L., L. H. Erikson, and R. G. Kvitek (2011), Small-scale sediment transport patterns and bedform morphodynamics: New insights from high-resolution multibeam bathymetry, *Geo-Mar. Lett.*, *31*, 227–236, doi:10.1007/s00367-011-0227-1.
Basu, S., and E. Foufoula-Georgiou (2002), Detection of nonlinearity and chaoticity in time series using the transportation distance function, *Phys. Lett. A*, *301*, 413–423.
Basu, S., E. Foufoula-Georgiou, B. Lashermes, and A. Arneodo (2007), Estimating intermittency exponent in neutrally stratified atmospheric surface layer flows: A robust framework based on magnitude cumulant analysis and surrogate analyses, *Phys. Fluids*, *19*, 115102.
Best, J. (2005), The fluid dynamics of river dunes: A review and some future research directions, *J. Geophys. Res.*, *110*, F04S02, doi:10.1029/2004JF000218.
Best, J., and J. Bridge (1992), The morphology and dynamics of low amplitude bedwaves upon upper stage plane beds and the preservation of planar laminae, *Sedimentology*, *39*, 737–752, doi:10.1111/j.1365-3091.1992.tb02150.x.
Blom, A., G. Parker, J. S. Ribberink, and H. J. de Vriend (2006), Vertical sorting and the morphodynamics of bed-form-dominated rivers: An equilibrium sorting model, *J. Geophys. Res.*, *111*, F01006, doi:10.1029/2004JF000175.
Butler, J. B., S. N. Lane, and J. H. Chandler (2001), Characterization of the structure of river-bed gravels using two-dimensional fractal analysis, *Math. Geol.*, *33*, 301–330, doi:10.1023/A:1007686206695.
Escauriaza, C., and F. Sotiropoulos (2011), Lagrangian model of bed-load transport in turbulent junction flows, *J. Fluid Mech.*, *666*, 36–76.
Hardy, R. J., S. N. Lane, R. I. Ferguson, and D. R. Parsons (2007), Emergence of coherent flow structures over a gravel surface: A numerical experiment, *Water Resour. Res.*, *43*, W03422, doi:10.1029/2006WR004936.
Hardy, R. J., J. L. Best, S. N. Lane, and P. E. Carbonneau (2009), Coherent flow structures in a depth-limited flow over a gravel surface: The role of near-bed turbulence and influence of Reynolds number, *J. Geophys. Res.*, *114*, F01003, doi:10.1029/2007JF000970.
Kantz, H., and T. Schreiber (1997), *Nonlinear Time Series Analysis*, Cambridge Univ. Press, Cambridge, U. K.
Keylock, C. J. (2006), Constrained surrogate time series with preservation of the mean and variance structure, *Phys. Rev. E*, *73*, 036707.
Keylock, C. J. (2007a), A wavelet-based method for surrogate data generation, *Physica D*, *225*, 219–228.

Keylock, C. J. (2007b), Identifying linear and non-linear behaviour in reduced complexity modelling output using surrogate data methods, *Geomorphology*, *90*, 356–366.
Keylock, C. J. (2008), Improved preservation of autocorrelative structure in surrogate data using an initial wavelet step, *Nonlin. Processes Geophys.*, *15*, 435–444.
Keylock, C. J. (2009), Evaluating the dimensionality and significance of "active periods" in turbulent environmental flows defined using Lipshitz/Hölder regularity, *Environ. Fluid Mech.*, *9*, 509–523.
Keylock, C. J. (2010), Characterizing the structure of nonlinear systems using gradual wavelet reconstruction, *Nonlin. Processes Geophys.*, *17*, 615–632.
Keylock, C. J. (2012), A resampling method for generating synthetic hydrological time series with preservation of cross-correlative structure and higher-order properties, *Water Resour. Res.*, *48*, W12521, doi:10.1029/2012WR011923.
Keylock, C. J., T. E. Tokyay, and G. Constantinescu (2011), A method for characterising the sensitivity of turbulent flow fields to the structure of inlet turbulence, *J. Turbul.*, *12*, N45, doi:10.1080/14685248.2011.636047.
Keylock, C. J., G. Constantinescu, and R. J. Hardy (2012c), The application of computational fluid dynamics to natural river channels: Eddy resolving versus mean flow approaches, *Geomorphology*, *179*, 1–20.
Keylock, C. J., A. Singh, and E. Foufoula-Georgiou (2013), The influence of migrating bed forms on the velocity-intermittency structure of turbulent flow over a gravel bed, *Geophys. Res. Lett.*, *40*, 1351–1355, doi:10.1002/grl.50337.
Kirkil, G., and G. Constantinescu (2010), Flow and turbulence structure around an in-stream rectangular cylinder with scour hole, *Water Resour. Res.*, *46*, W11549, doi:10.1029/2010WR009336.
Kolmogorov, A. N. (1941), The local structure of turbulence in incompressible viscous fluid for very large Reynolds numbers, *Dokl. Akad. Nauk SSSR*, *30*, 299–303.
Lacey, R. W. J., and A. G. Roy (2007), A comparative study of the turbulent flow field with and without a pebble cluster in a gravel bed river, *Water Resour. Res.*, *43*, W05502, doi:10.1029/2006WR005027.
Lawless, M., and A. Robert (2001), Scales of boundary resistance in coarse-grained channels: Turbulent velocity profiles and implications, *Geomorphology*, *39*, 221–238, doi:10.1016/S0169-555X(01)00029-0.
Lefebvre, A., V. B. Ernstsen, and C. Winter (2011), Influence of compound bedforms on hydraulic roughness in a tidal environment, *Ocean Dyn.*, *61*, 2201–2210, doi:10.1007/s10236-011-0476-6.
Lelouvetel, J., F. Bigillon, D. Doppler, I. Vinkovic, and J.-Y. Champagne (2009), Experimental investigation of ejections and sweeps involved in particle suspension, *Water Resour. Res.*, *45*, W02416, doi:10.1029/2007WR006520.
Moeckel, R., and B. Murray (1997), Measuring the distance between time series, *Physica D*, *102*, 187–194.
Nelson, P. A., J. G. Venditti, W. E. Dietrich, J. W. Kirchner, H. Ikeda, F. Iseya, and L. S. Sklar (2009), Response of bed surface patchiness to reductions in sediment supply, *J. Geophys. Res.*, *114*, F02005, doi:10.1029/2008JF001144.
Nikora, V., and J. Walsh (2004), Water-worked gravel surfaces: High-order structure functions at the particle scale, *Water Resour. Res.*, *40*, W12601, doi:10.1029/2004WR003346.
Nikora, V. I., D. G. Goring, and B. J. F. Biggs (1998), On gravel-bed roughness characterization, *Water Resour. Res.*, *34*, 517–527.
Paola, C., and R. Seal (1995), Grain-size patchiness as a cause of selective deposition and downstream fining, *Water Resour. Res.*, *31*, 1395–1407, doi:10.1029/94WR02975.
Parker, G., and C. M. Toro-Escobar (2002), Equal mobility of gravel in streams: The remains of the day, *Water Resour. Res.*, *38*(11), 1264, doi:10.1029/2001WR000669.
Parsons, D. R., J. L. Best, O. Orfeo, R. J. Hardy, R. Kostaschuk, and S. N. Lane (2005), Morphology and flow fields of three-dimensional dunes, Rio Parana, Argentina: Results from simultaneous multibeam echo sounding and acoustic Doppler current profiling, *J. Geophys. Res.*, *110*, F04S03, doi:10.1029/2004JF000231.
Parsons, D. R., J. L. Best, S. N. Lane, O. Orfeo, R. J. Hardy, and R. Kostaschuk (2007), Form roughness and the absence of secondary flow in a large confluence-diffluence, Rio Parana, Argentina, *Earth Surf. Process. Landforms*, *32*, 155–162.
Percival, D. B., and A. T. Walden (2000), *Wavelet Methods for Times Series Analysis*, Cambridge Univ. Press, Cambridge, U. K.
Poggi, D., A. Porporato, L. Ridolfi, J. D. Albertson, and G. G. Katul (2004), Interaction between large and small scales in the canopy sublayer, *Geophys. Res. Lett.*, *31*, L05102, doi:10.1029/2003GL018611.
Reesink, A. J. H., and J. S. Bridge (2007), Influence of superimposed bedforms and flow unsteadiness on formation of cross strata in dunes and unit bars, *Sediment. Geol.*, *202*, 281–296.
Reesink, A. J. H., and J. S. Bridge (2009), Influence of bedform superimposition and flow unsteadiness on the formation of cross strata in dunes and unit bars—Part 2, further experiments, *Sediment. Geol.*, *222*, 274–300.
Roy, A., T. Buffin-Bélanger, H. Lamarre, and A. Kirkbride (2004), Size, shape and dynamics of large-scale turbulent flow structures in a gravel-bed river, *J. Fluid Mech.*, *500*, 1–27.
Schreiber, T., and A. Schmitz (1996), Improved surrogate data for nonlinearity tests, *Phys. Rev. Lett.*, *77*, 635–638.
Schreiber, T., and A. Schmitz (1997), Discrimination power of measures for nonlinearity in a time series, *Phys. Rev. E*, *55*, 5443–5447.
Simons, D. B., E. V. Richardson, and C. F. Nordin Jr. (1965), Bedload equation for ripples and dunes, *U.S. Geol. Surv. Prof. Pap.*, *462-H*, U.S. Gov. Print. Off., Washington, D. C.
Singh, A., K. Fienberg, D. J. Jerolmack, J. Marr, and E. Foufoula-Georgiou (2009a), Experimental evidence for statistical scaling and intermittency in sediment transport rates, *J. Geophys. Res.*, *114*, F01025, doi:10.1029/2007JF000963.
Singh, A., S. Lanzoni, and E. Foufoula-Georgiou (2009b), Nonlinearity and complexity in gravel bed dynamics, *Stochastic Environ. Res. Risk Assess.*, *23*, 967–975.
Singh, A., F. Porté-Agel, and E. Foufoula-Georgiou (2010), On the influence of gravel bed dynamics on velocity power spectra, *Water Resour. Res.*, *46*, W04509, doi:10.1029/2009WR008190.
Singh, A., S. Lanzoni, P. R. Wilcock, and E. Foufoula-Georgiou (2011), Multiscale statistical characterization of migrating bed forms in gravel and sand bed rivers, *Water Resour. Res.*, *47*, W12526, doi:10.1029/2010WR010122.
Singh, A., E. Foufoula-Georgiou, F. Porte-Agel, and P. R. Wilcock (2012), Coupled dynamics of the co-evolution of gravel bed topography, flow turbulence and sediment transport in an experimental channel, *J. Geophys. Res.*, *117*, F04016, doi:10.1029/2011JF002323.
Smith, N. D. (1972), Some sedimentological aspects of planar cross-stratification in a sandy braided river, *J. Sediment. Petrol.*, *42*, 624–634.
Takens, F. (1981), Detecting strange attractors in turbulence, *Lect. Notes Math.*, *898*, 366–381.
Theiler, J., S. Eubank, A. Longtin, B. Galdrikian, and J. D. Farmer (1992), Testing for nonlinearity in time series: The method of surrogate data, *Physica D*, *58*, 77–94.
van Balen, W., K. Blanckaert, and W. S. J. Uijttewaal (2010), Analysis of the role of turbulence in curved open-channel flow at different water depths by means of experiments, LES and RANS, *J. Turbul.*, *11*, 1–34.

Venditti, J. G. (2007), Turbulent flow and drag over fixed two- and three-dimensional dunes, *J. Geophys. Res.*, *112*, F04008, doi:10.1029/2006JF000650.

Venditti, J. G., and S. J. Bennett (2000), Spectral analysis of turbulent flow and suspended sediment transport over fixed dunes, *J. Geophys. Res.*, *105*, 22,035–22,047.

von Kárman, T., and L. Howarth (1938), On the statistical theory of turbulence, *Proc. R. Soc. London, Ser. A*, *164*, 192–215.

Wathen, S. J., R. I. Ferguson, T. B. Hoey, and A. Werritty (1995), Unequal mobility of gravel and sand in weakly bimodal river sediments, *Water Resour. Res.*, *31*, 2087–2096.

Wilcock, P. R., S. T. Kenworthy, and J. C. Crowe (2001), Experimental study of the transport of mixed sand and gravel, *Water Resour. Res.*, *37*, 3349–3358, doi:10.1029/2001WR000683.

Wu, Y., and K. T. Christensen (2010), Spatial structure of a turbulent boundary layer with irregular surface roughness, *J. Fluid Mech.*, *655*, 380–418.

Zedler, E. A., and R. L. Street (2001), Large-Eddy Simulation of sediment transport: Currents over ripples, *J. Hydraul. Eng.*, *127*, 444–452.